Electronic Supplementary Material (ESI) for Journal of Materials Chemistry C.

Supporting Information

High-performance near-infrared photodetectors based on C_3N quantum dots integrated with single-crystal graphene

Yun Zhao[a,b], Xiaoqiang Feng[b], Menghan Zhao[b], Xiaohu Zheng[c], Zhiduo Liu[d], Siwei Yang[e,*], Shiwei Tang[b], Da Chen[b], Gang Wang[b,*], and Guqiao Ding[b,e]

[a]Faculty of Electrical Engineering and Computer Science, Ningbo University, Ningbo 315211, P. R. China.

[b]Department of Microelectronic Science and Engineering, School of Physical Science and Technology, Ningbo University, Ningbo 315211, P. R. China.

[c]Beijing Academy of Quantum Information Sciences, Beijing 100193, P. R. China.

[d]State Key Laboratory of Integrated Optoelectronics, Institute of Semiconductors, Chinese Academy of Sciences, Beijing 100083, P. R. China.

[e]State Key Laboratory of Functional Materials for Informatics, Shanghai Institute of Microsystem and Information Technology, Chinese Academy of Sciences, Shanghai 200050, P. R. China.

*Correspondence to: gangwang@nbu.edu.cn (G. Wang); yangsiwei@mail.sim.ac.cn (Siwei Yang)

I. Characterization of C_3N QDs.

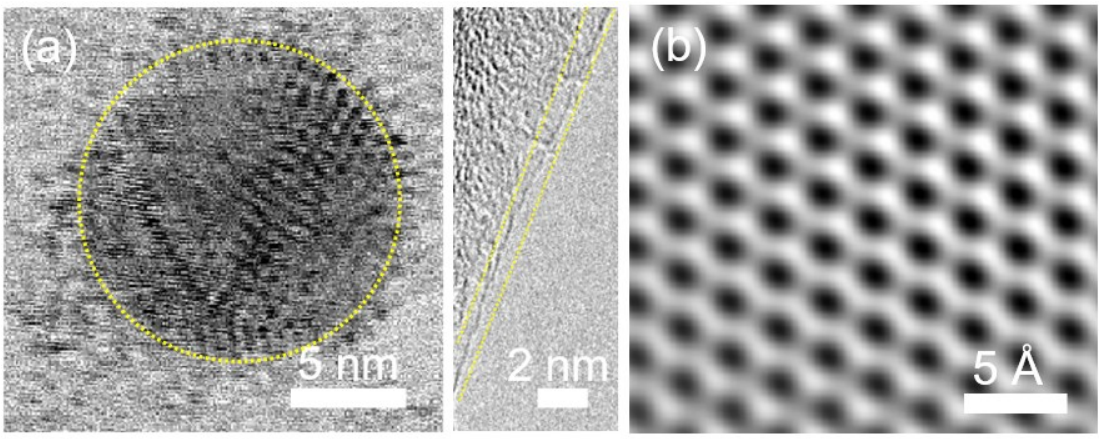

Fig. S1. (a) HR-TEM image of the C_3N QDs. (b) The high-angle annular dark field-STEM image of the C_3N QD.

The monolayer feature is confirmed by high-resolution transmission electron microscopy (HR-TEM), as shown in **Fig. S1 (a)**. The suspended the C_3N QDs on the TEM grids and the HR-TEM image randomly taken from numerous C_3N QDs edges exhibits the single layer characteristics reveals. A high-angle annular dark field-STEM image taken from C_3N QD shows the well-crystallized graphene liked honeycomb structure, as shown in **Fig. S1 (b)**.

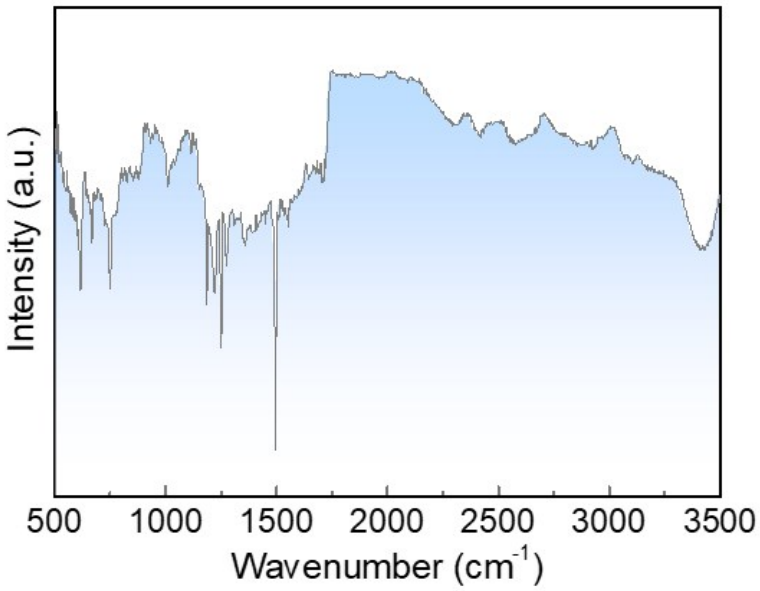

Fig. S2. Chemical structure analysis of C_3N QDs: FT-IR of C_3N QDs.

The fourier transform infrared (FT-IR) spectrum of C_3N QDs is shown in **Fig. S2**, the peak at 3488 cm^{-1} can be due to the N-H asymmetric stretching vibration of -NH_2 age groups. The peak at 1601 cm^{-1} may be due to the C=C and C=N stretching in phenazine structure. The peak at 1500 cm^{-1} may be due to the N-H in-plane deformation in parahelium structure. The peak at 1337 cm^{-1} may be due to the C-N stretching vibration in parahelium structure. The peak at 1220 cm^{-1} may be due to the C-N stretching vibration in parahelium structure. The peak at 1131 cm^{-1} may be due to the N-H out-of-plane deformation in parahelium structure. The peak at 758 cm^{-1} may be due to the 2,4,6-trisubstituted (phenazine structure) ring deformation vibration.

II. The spectral response characteristics of the device.

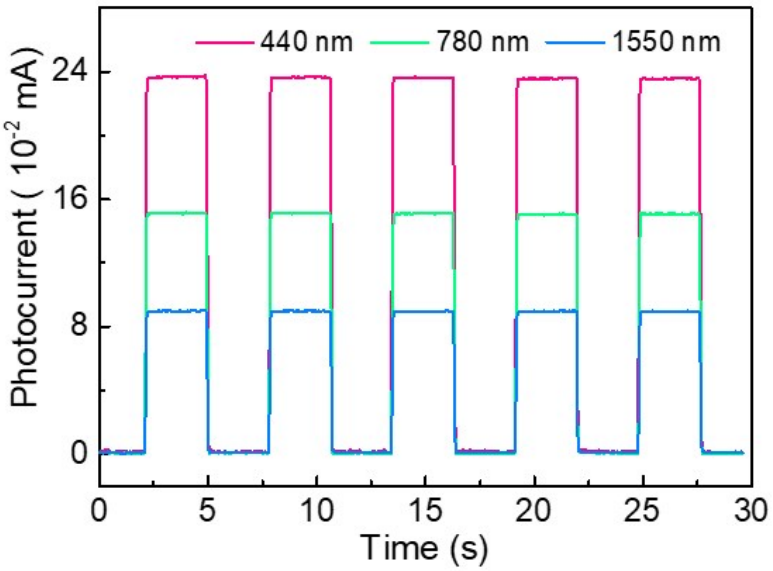

Fig. S3. The photocurrents under 440 nm, 780 nm, and 1550 nm light illumination (V_{DS} = 30 mV and V_{BG} = 0 V). The light intensity is fixed at 40 mW/cm^2.

The performance of photodetectors measured under light illumination with variable wavelengths (440, 780, and 1550 nm) have been measured during the preparation of the manuscript. The photo-response of photodetector based on the hybrid graphene and C_3N QDs is assessed with variable wavelengths as depicted in **Fig. S3**. It clearly shows that when decreasing the wavelength from 1550 nm to 440 nm, the

photocurrents increase from 89 μA to 238 μA, which can be attributed to the increment of photo-generated electron-hole pairs motivated by higher photon energy.[1-3]

III. The concentration of C_3N QDs affect the photo-response properties of the photodetectors.

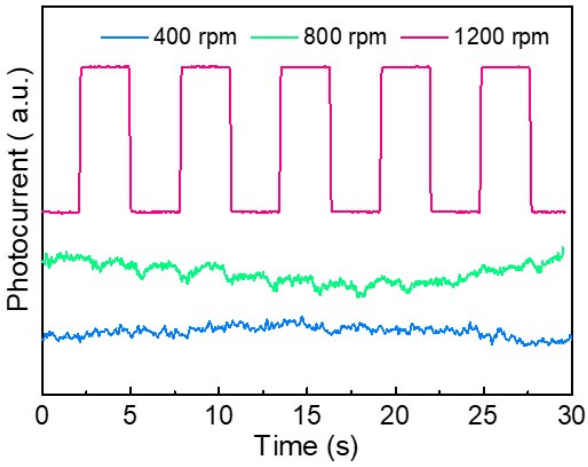

Fig. S4. Photo-switching curves of the photodetector in response to pulsed light illumination with the variable concentration of C_3N QDs integrated with single-crystal graphene.

The concentration of C_3N QDs integrated with single-crystal graphene can be accurately governed by tuning C_3N QDs spin-coat speed. The switching behavior depends on the variable concentration of C_3N QDs integrated with single-crystal graphene, as exhibited in **Fig. S4**. In detail, as the spin-coat speed is decreased from 1200 to 400 rpm, the switching behavior preserves for the light illumination with the wavelength of 1550 nm, but the reproducibility and stability become worse. With regard to 400 rpm, no switching behavior is observed for the light illumination. The degraded switching behavior for low spin-coat speed is attributed to weakened the quantum confinement effect and edge effect for C_3N QDs.[4-7]

IV. The size of C_3N QDs affect the photo-response properties of the photodetectors.

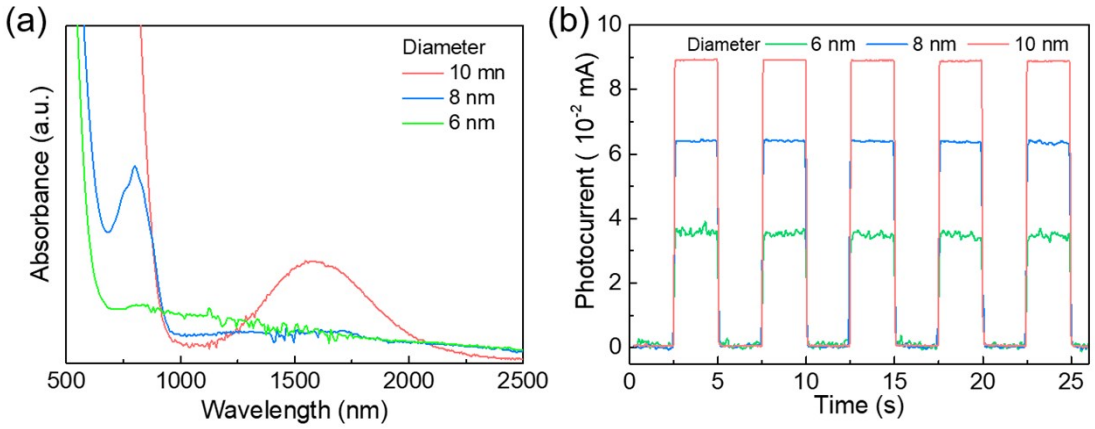

Fig. S5. (a) Uv-visible near-infrared absorption spectrophotometry of C_3N QDs with different diameter. (b) The photocurrents of three samples under 1550 nm light illumination (V_{DS} = 30 mV and V_{BG} = 0 V). The light intensity is fixed at 40 mW/cm^2.

We have successfully synthesized C_3N QDs with the different diameters (10 nm, 8 nm, and 6 nm). **Fig. S5 (a)** shows the Uv-vis near-infrared absorption spectrum of C_3N QDs with different size. Obviously, C_3N QDs with diameter of 10 nm show strong absorption at ca. 1550 nm. This can be due to the large size of C_3N QDs. By contrast, due to the quantum size effect, C_3N QDs with diameter of 8 nm and 6 nm show much weak absorption at ca. 1550 nm. When decreasing the sizes of C_3N QDs from 10 nm to 6 nm, the photocurrents gradually decline, as shown in **Fig. S5 (b)**, which can be attributed to the reduced intensity of electron-hole pairs since the hole-electron pairs need to be generated by light-illumination in the C_3N QDs.[8-10]

V. The responsivity (R) and specific detectivity (D*) measurement.

The responsivity (R) and specific detectivity (D*) can be calculated as follow:

The R is expressed by the equation:[11]

$$R = I_{ph}/P_{light}$$

Where I_{ph} is the photocurrent and P_{light} is the incident-light power, respectively. I_{ph} is 90 μA. The illumination power is 40 mW/cm^2.

And D* is given by:[12]

$$D^* = (A\Delta f)^{1/2} \times R/i_n$$

Where A is the effective area of a photodetector (the beam spot size is 2 μm for photoresponsivity measurement and the light focus only on the entire device channel), Δf is the electrical bandwidth, and i_n is the noise current. The noise current is determined mainly by dark current (I_{dark}) (I_{dark} is 9 nA), and the dark current noise can also be calculated from the following equation:[13-14]

$$i_n = (2eI_{dark}\Delta f)^{1/2}$$

$$D^* = (A/2eI_{dark})^{1/2} \times R$$

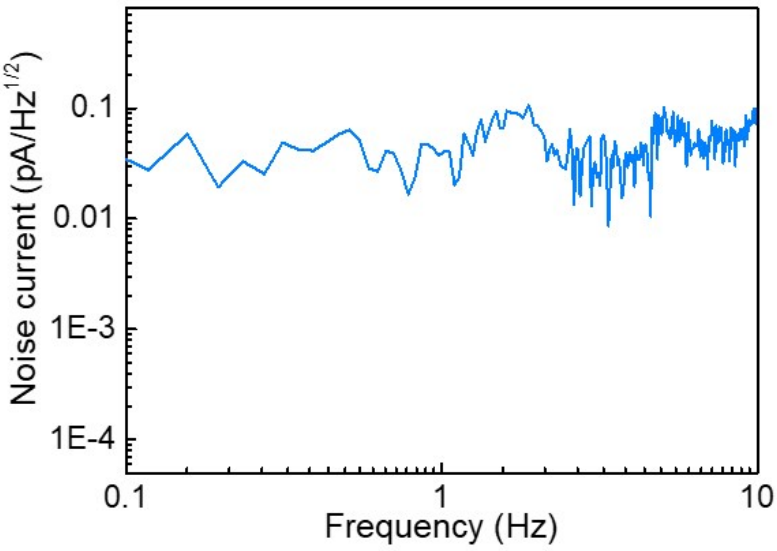

Fig. S6. Noise current spectral density measured under ambient condition.

To obtain the specific detectivity, we must obtain the dark current noise. Generally, it can be measured directly using the Fast Fourier Transform (FFT) algorithm method. We measured the dark current using a preamplifier with a sampling rate of 10 kHz, and the data were analyzed with FFT software. As shown in **Fig. S6**, based on dark current of the device at 0 V, the measured dark current noise is 2.9 fA $Hz^{-1/2}$ at 1 Hz, and the resulting specific detectivity is 1.2×10^{14} cm $Hz^{1/2}$ W^{-1} considering the device working area of 4 μm^2, when the light intensity is 40 mW/cm^2.

References

[1] S. C. Qin, F. Q. Wang, Y. J. Liu, Q Wan, X. R. Wang, Y. B. Xu, Y. Shi, X. M. Wang, R. Zhang, 2D Mater., 2017, **4**, 035022.

[2] W. G. Tu, Y. Zhou, Q. Liu, S. C. Yan, S. S. Bao, X. Y. Wang, M. Xiao, Z. G. Zou, Adv. Funct. Mater., 2013, **23**, 1743-1749.

[3] M. A. Huber, F. Mooshammer, M. Plankl, L. Viti, F. Sandner, L. Z. Kastner, T. Frank, J. Fabian, M. S. Vitiello, T. L. Cocker, R. Huber, Nat. Nanotechnol., 2017, **12**, 207-211.

[4] Y. Li, Y. Hu, Y. Zhao, G. Q. Shi, L. E. Deng, Y. B. Hou, L. T. Qu, Adv. Mater., **23**, 776-780.

[5] D. Y. Pan, J. C. Zhang, Z. Li, M. H. Wu, Adv. Mater., 2010, **22**, 734-738.

[6] A. D. Guclu, P. Potasz, P. Hawrylak, Phys. Rev. B, 2010, **82**, 155445.

[7] S. Kim, S. W. Hwang, M. K. Kim, D. Y. Shin, D. H. Shin, C. O. Kim, S. B. Yang, J. H. Park, E. Hwang, S. H. Choi, G. Ko, S. Sim, C. Sone, H. J. Choi, S. Bae, B. H. Hong, ACS Nano, 2012, **6**, 8203-8208.

[8] P. P. Yu, K. Hu, H. Y. Chen, L. X. Zheng, X. S. Fang, Adv. Funct. Mater., 2017, **27**, 1703166.

[9] G. Konstantatos, M. Badioli, L. Gaudreau, J. Osmond, M. Bernechea, F. P. Arquer, F. Gatti, F. H. L. Koppens, Nat. Nanotechnol., 2012, **7**, 363-368.

[10] I. Goykhman, U. Sassi, B. Desiatov, N. Mazurski, S. Milana, D. D. Fazio, A. Eiden, J. Khurgin, J. Shappir, U. Levy, A. C. Ferrari, Nano Lett., 2016, **16**, 3005-3013.

[11] A. Q. Hu, H. J.Tian, Q. L. Liu, L. Wang, L. Wang, X. Y. He, Y. Luo, X. Guo, Adv. Opt. Mater., 2019, **7**, 1801792.

[12] Q. L. Liu, H. J. Tian, J. W. Li, A. Q. Hu, X. Y. He, M. L. Sui, X. Guo, Adv. Opt. Mater., 2019, **7**, 1900455.

[13] H. Ali, Y. Y. Zhang, J. Tang, K. Peng, S. B. Sun, Y. Sun, F. L. Song, A. Falak, S. Y. Wu, C. J. Qian, M. Wang, Z. C. Zuo, K. J. Jin, A. M. Sanchez, H. Y. Liu, X. L. Xu, Small, 2018, **14**, 1704429.

[14] M. J. Grotevent, C. U. Hail, S. Yakunin, D. N. Dirin, K. Thodkar, G. B. Barin, P. G. Sionnest, M. Calame, D. Poulikakos, M. V. Kovalenko, I. Shorubalko, Adv. Opt. Mater., 2019, **7**, 1900019.